The Astrophysical Journal, 940:105 (10pp), 2022 December 1 https://doi.org/10.3847/1538-4357/ac94cf

Discovery of Year-scale Time Variability from Thermal X-Ray Emission in Tycho's Supernova Remnant

Masamune Matsuda[1], Hiroyuki Uchida[1], Takaaki Tanaka[2], Hiroya Yamaguchi[3,4], and Takeshi Go Tsuru[1]
[1] Department of Physics, Kyoto University, Kitashirakawa Oiwake, Sakyo, Kyoto, Kyoto 606-8502, Japan; matsuda.masamune.38a@kyoto-u.jp
[2] Department of Physics, Konan University, 8-9-1 Okamoto, Higashinada, Kobe, Hyogo 658-8501, Japan
[3] Institute of Space and Astronautical Science (ISAS), Japan Aerospace Exploration Agency (JAXA), 3-1-1 Yoshinodai, Chuo, Sagamihara, Kanagawa 252-5210, Japan
[4] Department of Physics, The University of Tokyo, 7-3-1 Hongo, Bunkyo, Tokyo 113-0033, Japan
Received 2022 March 16; revised 2022 September 21; accepted 2022 September 22; published 2022 November 25

Abstract

Mechanisms of particle heating are crucial to understanding the shock physics in supernova remnants (SNRs). However, there has been little information on time variabilities of thermalized particles so far. Here, we present a discovery of a gradually brightening thermal X-ray emission found in the Chandra data of Tycho's SNR obtained during 2000–2015. The emission exhibits a knot-like feature (Knot1) with a diameter of $\simeq$0.04 pc located in the northwestern limb, where we also find localized Hα filaments in an optical image taken with the Hubble Space Telescope in 2008. The model with the solar abundance reproduces the spectra of Knot1, suggesting that Knot1 originates from the interstellar medium; this is the first detection of thermal X-ray emission from swept-up gas found in Tycho's SNR. Our spectral analysis indicates that the electron temperature of Knot1 has increased from $\sim$0.30 to $\sim$0.69 keV within the period between 2000 and 2015. These results lead us to ascribe the time-variable emission to a small dense clump recently heated by the forward shock at the location of Knot1. The electron-to-proton temperature ratio immediately downstream of the shock ($\beta_0 \equiv T_e/T_p$) is constrained to be $m_e/m_p \leqslant \beta_0 \leqslant 0.15$ to reproduce the data, indicating the collisionless electron heating with efficiency is consistent with previous Hα observations of Tycho and other SNRs with high shock velocities.

Unified Astronomy Thesaurus concepts: Supernova remnants (1667); X-ray sources (1822); Interstellar medium (847); Interstellar thermal emission (857); Plasma astrophysics (1261)

1. Introduction

The physics of collisionless shocks is an intriguing topic since they are involved with a number of unsettled problems, e.g., the evolution of magnetic turbulence, the electron heating mechanism, and the process of cosmic-ray acceleration. One poorly understood process among them is collisionless electron heating, although it is an important subject that might be related to the formation of the collisionless shocks. While several pieces of observational evidence for collisionless heating have been found in various astrophysical environments, such as solar wind shocks (Schwartz et al. 1988), supernova remnants (SNRs; e.g., Laming et al. 1996; Ghavamian et al. 2001; Yamaguchi et al. 2014), and merging galaxy clusters (e.g., Markevitch et al. 2005; Russell et al. 2012), the detailed heating mechanism in collisionless shocks is still under debate.

The temperature change at the shock front provides a clue to the elusive fundamental properties of the collisionless electron heating. When electron heating occurs without a collisionless process, such as plasma wave heating via Buneman instabilities (e.g., Cargill & Papadopoulos 1988) and lower hybrid wave heating (e.g., Laming 2000), the temperature downstream of the shock with a velocity of $v_{\rm sh}$ is written as $kT_i = (3/16) m_i v_{\rm sh}^2$, where k is the Boltzmann constant, and m_i is the mass of particle species i. It follows that the particle temperature in the shock transition is proportional to its mass. Thus, the electron temperature is much smaller than the temperature of heavier ions. The electrons then receive thermal energy from the ions via Coulomb collisions, and the temperature gradually increases. On the other hand, when the collisionless heating is efficient, the electron temperature rises quickly in the shock transition and gradually rises via Coulomb collisions further downstream (e.g., McKee 1974; Cargill & Papadopoulos 1988). Direct measurement of these temperature changes can constrain the efficiency of collisionless heating in a shock transition.

Recent observations found year-scale time variabilities of synchrotron X-rays in small scales in shock waves of young SNRs: RX J1713.7-3946 (Uchiyama et al. 2007), Cassiopeia A (Cas A; Uchiyama & Aharonian 2008), and G330.2+1.0 (Borkowski et al. 2018). Our previous studies also revealed similar year-scale spectral changes in one of the youngest and nearby Type Ia SNRs, Tycho's SNR (hereafter, Tycho; Okuno et al. 2020; Matsuda et al. 2020). These studies provided us with important information on a real-time energy change of nonthermal particles. On the other hand, time variabilities of thermal X-rays, which help us solve the problem of the heating mechanism of thermalized particles, have been less reported except for several examples on Cas A (e.g., Patnaude & Fesen 2007, 2014; Rutherford et al. 2013) and SN 1987A (e.g., Sun et al. 2021; Ravi et al. 2021).

Tycho has bright synchrotron X-ray rims with thermalized ejecta, in which Yamaguchi et al. (2014) revealed evidence of collisionless heating based on Fe-K diagnostics. Although thermal X-ray emission from Tycho has been detected only from the ejecta heated by the reverse shock (e.g., Hwang et al. 2002), some studies suggested that the forward shock interacted with dense materials, as evidenced by Hα observations

Table 1
Observation Log

ObsID	Start Date	Effective Exposure (ks)	Chip
115	2000 Oct 01	49	ACIS-S
3837	2003 Apr 29	146	ACIS-I
7639	2007 Apr 23	109	ACIS-I
8551	2007 Apr 26	33	ACIS-I
10093	2009 Apr 13	118	ACIS-I
10094	2009 Apr 18	90	ACIS-I
10095	2009 Apr 23	173	ACIS-I
10096	2009 Apr 27	106	ACIS-I
10097	2009 Apr 11	107	ACIS-I
10902	2009 Apr 15	40	ACIS-I
10903	2009 Apr 17	24	ACIS-I
10904	2009 Apr 13	35	ACIS-I
10906	2009 May 03	41	ACIS-I
15998	2015 Apr 22	147	ACIS-I

(e.g., Ghavamian et al. 2000; Lee et al. 2010) and velocity measurements of X-ray shells (Tanaka et al. 2021). These results imply a presence of interstellar medium (ISM) heated very recently by the forward shock. We, therefore, search for the thermal X-ray radiation from forward-shocked ISM and then investigate its temperature evolution through observations of short timescale thermal variability using multiple archival Chandra data sets. Throughout this paper, we adopt $\simeq$2.5 kpc as the distance to Tycho (Zhou et al. 2016), and the statistical errors are quoted at the 1σ level.

2. Observations and Data Reduction

Tycho was observed with the Chandra X-ray Observatory using ACIS-S in 2000 and ACIS-I in 2003, 2007, 2009, and 2015. Table 1 presents the observation log. We reprocess all of the data with the Chandra Calibration Database (CALDB) version 4.8.2. For the relative astrometry corrections, we align the coordinates of each observation to that of the data set with ObsID = 10095, which has the longest effective exposure time. We first detect point sources in the field using the CIAO task `wavdetect`. We then reprocess all of the event files using the tasks `wcs_match` and `wcs_update`. Because the accuracy of the frame alignment depends on the photon statistics, short time observations (ObsID: 8551, 10903, 10904, and 10906) are discarded for the above astrometry and used only for spectral analysis.

3. Analysis and Results

3.1. Imaging Analysis

To search for time variabilities of thermal emissions, we make a difference map by subtracting an exposure-corrected image taken in 2003 from one taken in 2015. Since the thermal emission dominates in a soft band in most regions (e.g., Warren et al. 2005; Sato & Hughes 2017), we first focus on the lowest energy band (0.5–1.5 keV) as shown in Figure 1. The figure shows the flux change of thermal emission in the interior of the shell beside nonthermal emission at the shell. Most features in the difference map show the flux increase and decrease next to each other. These features result from bright structures moving between 2000 and 2015 due to expanding ejecta and radial proper motions of the blast waves. In the northeast, however, we discover a bright spot (hereafter, Knot1) whose photon count monotonically increases over time with no signs of proper motion (panel (b) of Figure 1).

Figure 2 shows visual comparisons of flux images of Knot1 in the soft (0.5–1.5 keV), the middle (1.6–2.5 keV), and the hard (4.0–6.0 keV) bands. For better statistics, the images in 2009 are created by adding together the observations of ObsIDs 10093, 10094, 10095, 10096, 10097, and 10902 after the astrometry corrections (see Section 2). We confirm in Figure 2(a) that Knot1 was gradually brightening from 2000 through 2015. On the other hand, Figure 2(b) shows no significant flux fluctuation but for the ejecta expansion, suggesting that Knot1 has a different origin from the middle band X-rays. We also find that the synchrotron emission is relatively faint in Knot1 without any significant flux changes (Figure 2(c)), unlike the "stripe" regions in the southwest (SW; Okuno et al. 2020; Matsuda et al. 2020).

3.2. Spectral Analysis

In order to investigate the nature of Knot1 and quantitatively measure its time variability, we analyze spectra extracted from the region shown in Figure 2. The data sets obtained in each year are merged; we thus obtain five spectra from five different epochs (2000, 2003, 2007, 2009, and 2015). A background spectrum is extracted from a blank region outside of the remnant. To estimate the contribution from the emission in the energy above the middle band in Knot1, we also extract spectra from a nearby reference region (noted as "Ref1" in Figure 2), where the flux of the middle band component is almost the same as in Knot1.

Comparing the Knot1 spectra with the best-fit model of Ref1, we reveal that the Knot1 emission in the $\lesssim$1.5 keV band is significantly brighter than that of Ref1 while not in the $\gtrsim$1.5 keV band (Figure 3). The thermal radiation in Ref1 is likely to have the same origin as the southeastward diffusing ejecta since the ejecta emission generally dominates the thermal radiation in the innermost region of the remnant (e.g., Cassam-Chenaï et al. 2007; Miceli et al. 2015). This is supported by its spectrum, which can be reproduced by a pure-metal non-equilibrium ionization (NEI) model. Thus, it is plausible to interpret that the excess emission of Knot1 in the soft band is due to the radiation from the knot structure. The figure reveals that the energy band with the high Knot1/Ref1 ratio extends to higher energy year by year, supporting the flux increase in the soft band of Knot1. To estimate the time variability in the soft band more quantitatively, we model the spectra of Knot1 with a soft component added to the Ref1 model.

We simultaneously fit the spectra of the Knot1 and the Ref1 region taken in 2000, 2003, 2007, 2009, and 2015. The spectrum of Ref1 is modeled with an absorbed NEI plus a power law according to previous studies (e.g., Yamaguchi et al. 2017). For the following analysis, we use version 12.10.1f of XSPEC (Arnaud 1996) with AtomDB version 3.0.9 (Foster et al. 2017). The NEI components represent the ejecta of the remnant. The electron temperatures (kT_e), ionization age (n_et), and abundances of these components are assumed to be shared for each year. Because Tycho is a remnant of Type Ia SN, H, He, and N are assumed to be absent in the ejecta. O and Ne are fixed at the solar value with respect to C, whose atomic number is the lowest in the element of the ejecta. The abundance of the other elements is free. The emission measure (EM) is defined as $\int n_e n_C dV/4\pi d^2 [C/H]_\odot$, where n_e and n_C are the number

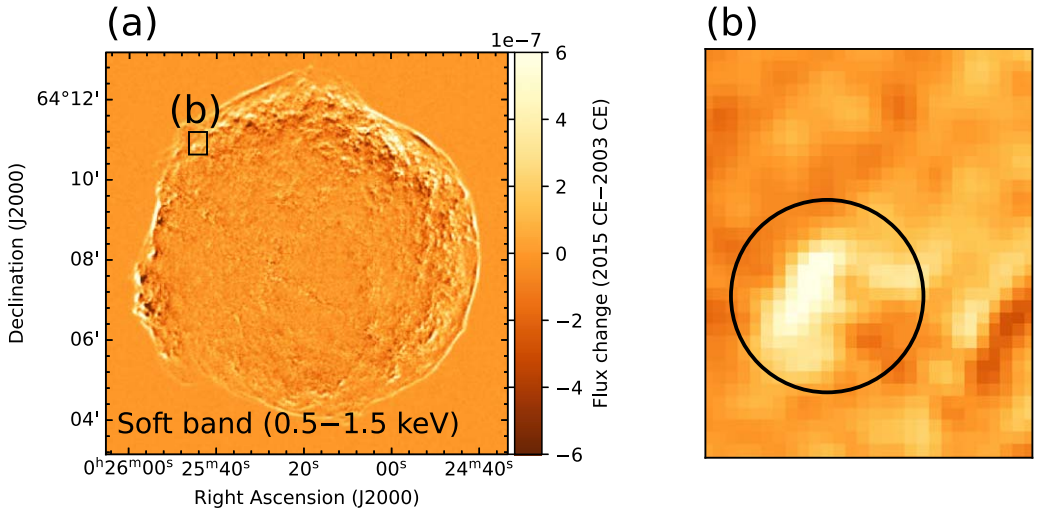

Figure 1. (a) Difference image of Tycho between 2003 and 2015 in the 0.5–1.5 keV band, where Ne-Kα and Fe-L lines are dominated. The unit for the color scale is photons s^{-1} cm^{-2}. Knot1 is located in the box region. (b) Enlarged image of the box region indicated in panel (a). The circle is the region where the flux changes significantly.

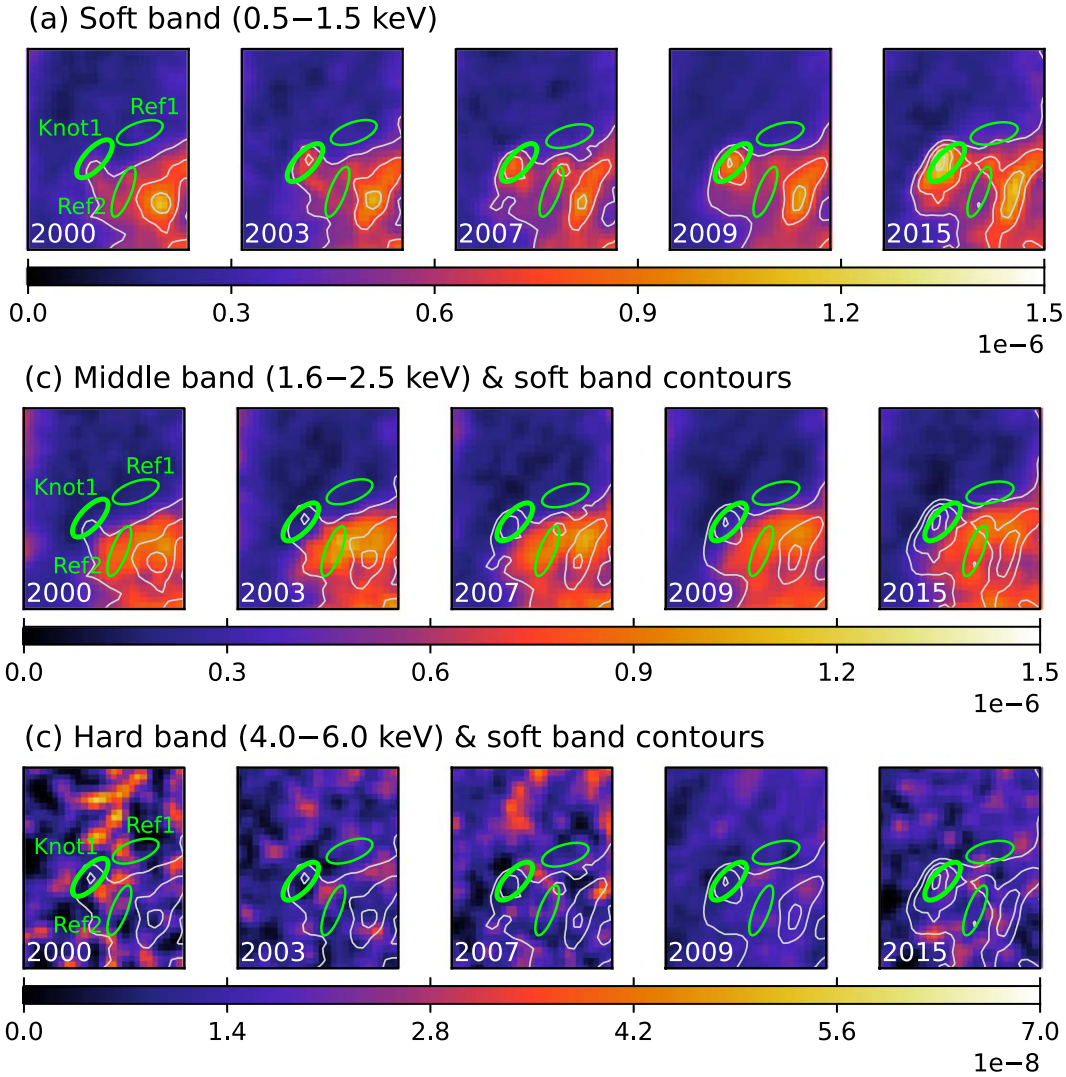

Figure 2. Soft (a), middle (b), and hard (c) band X-ray images around Knot1 taken in 2000, 2003, 2007, 2009, and 2015. All of the images are exposure corrected. In all of the panels, the unit for the color scale is photons s^{-1} cm^{-2}. Contours represent the flux of the soft-band X-rays. The green ellipses are the Knot1, Ref1, and Ref2 regions used for spectral extraction, respectively.

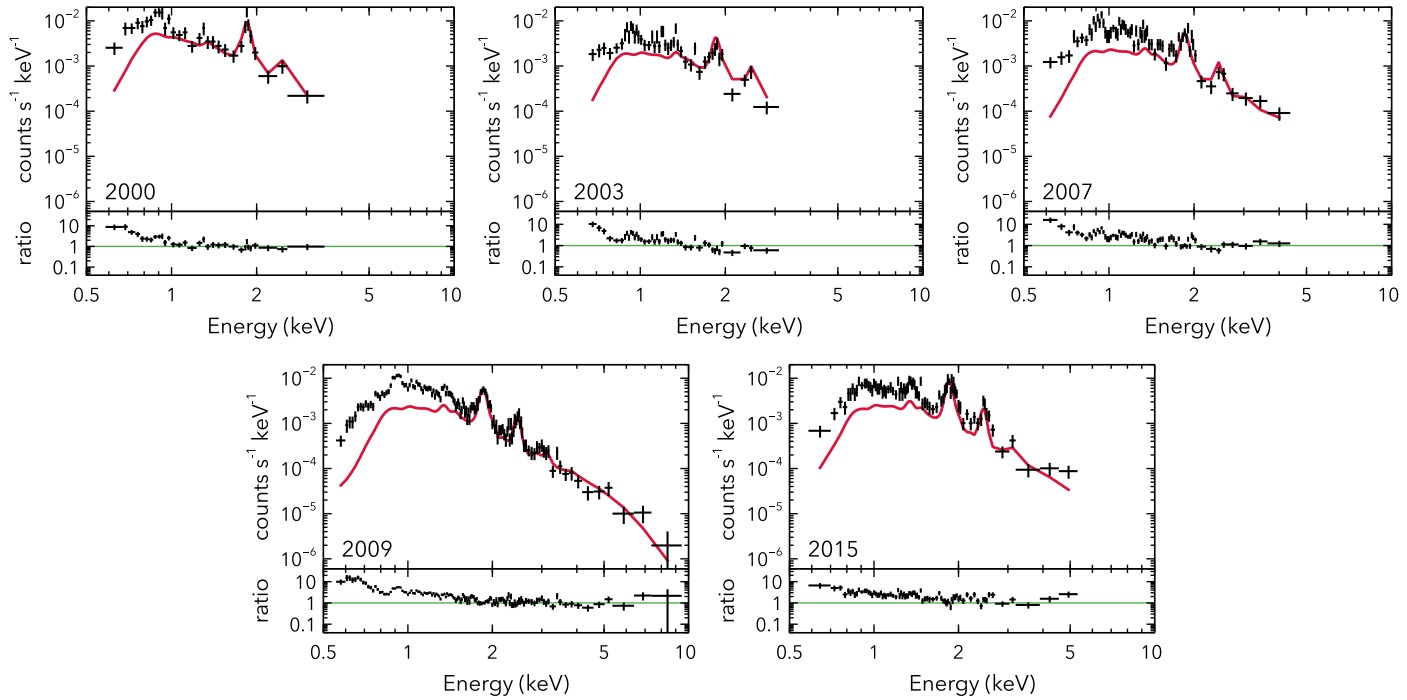

Figure 3. Comparison of the spectra of Knot1 (black) and the best-fit model of Ref1 for the effective area of Knot1 (red) in 2000, 2003, 2007, 2009, and 2015. The model is composed of an NEI component and a power-law component as explained in the text. Lower panels in each box show the ratio of the data of Knot1 to the model of Ref1.

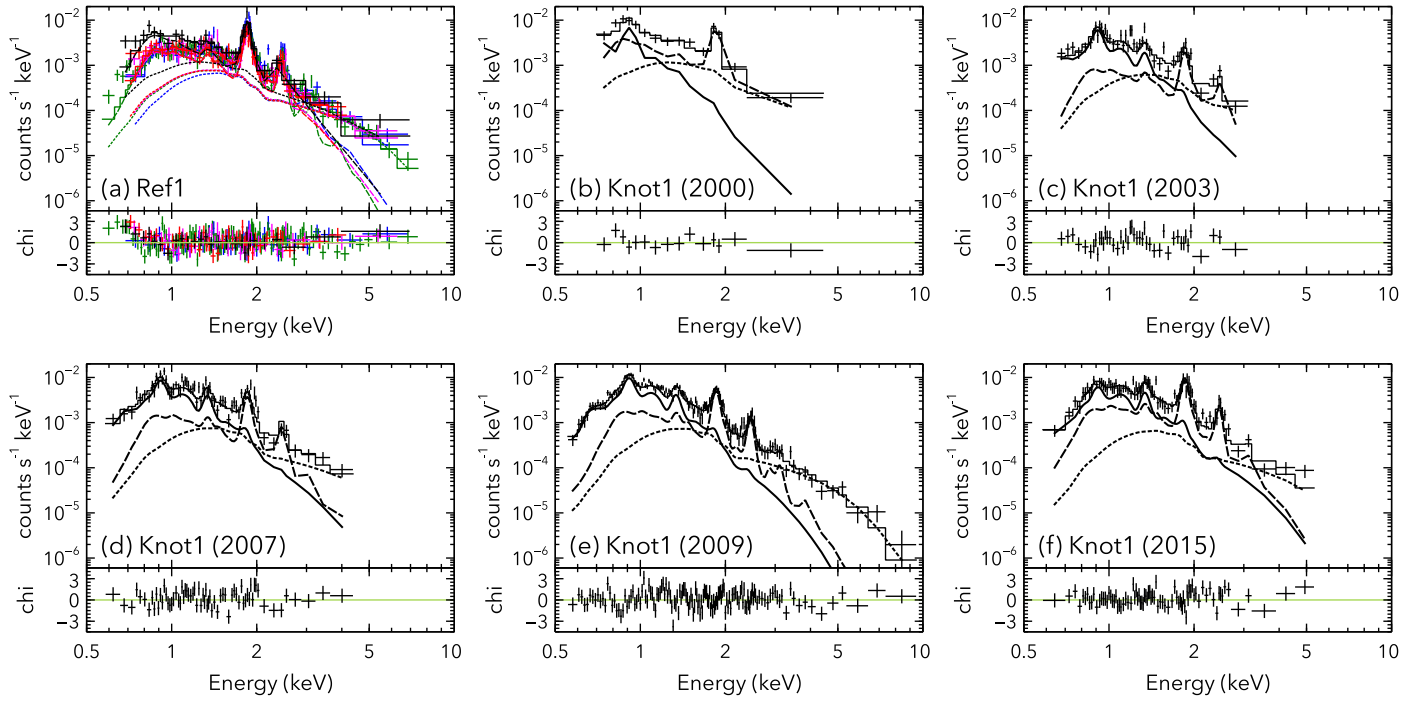

Figure 4. (a) Spectra of Ref1 taken in 2000 (black), 2003 (red), 2007 (magenta), 2009 (green), and 2015 (blue). The best-fit models are shown as the stepped lines. The dashed line and dotted line are the NEI component and the nonthermal component, respectively. (b)–(f) Spectra of Knot1 taken in 2000, 2003, 2007, 2009, and 2015. The solid lines are the soft components. The other lines represent the same components as panel (a).

densities of electrons and carbon, and V is the volume of the emitting plasma. The photon index of the power law is fixed to 2.79, which is the value obtained from a nearby nonthermal-dominated region. The normalization of the power laws in 2000, 2003, 2007, 2009, and 2015 are linked to each other. We applied the Tübingen–Boulder model (Wilms et al. 2000) for the interstellar absorption. The result of the spectral fit and best-fit parameters of the Ref1 region are shown in Figure 4(a) and Table 2, respectively.

We fit the Knot1 spectra with a model consisting of the Ref1 component and an additional soft component. The NEI model is used for the soft component. The abundances of each element are fixed to the solar value. Values of n_et in years other than 2000, kT_e, and EMs are set as free parameters. Only n_et in

Table 2
Best-fit Parameters of Ref1 and Knot1 Regions

Components	Parameters (Units)	2000	2003	2007	2009	2015
Absorption	$N_{\rm H}$ (10^{22} cm^{-2})			$1.01^{+0.04}_{-0.03}$		
Ref1 region						
NEI comp.	EM[a] (10^{9} cm^{-5})	$2.4^{+1.3}_{-1.1}$	$1.6^{+1.4}_{-1.2}$	$2.3^{+1.3}_{-1.2}$	$3.0^{+1.4}_{-1.2}$	$5.2^{+2.2}_{-2.0}$
	kT_e (keV)			0.70 ± 0.03		
	n_et (10^{11} cm^{-3} s)			$5.0^{+1.3}_{-1.2}$		
	[Mg/C]/[Mg/C]$_\odot$			$1.4^{+0.8}_{-0.4}$		
	[Si/C]/[Si/C]$_\odot$			11^{+5}_{-3}		
	[S/C]/[S/C]$_\odot$			11^{+6}_{-3}		
	[Ar/C]/[Ar/C]$_\odot$(=[Ca/C]/[Ca/C]$_\odot$)			9^{+6}_{-4}		
	[Fe/C]/[Fe/C]$_\odot$(=[Ni/C]/[Ni/C]$_\odot$)			$1.1^{+0.8}_{-0.4}$		
Power law	Γ			2.79 (fixed)		
	Flux[b] (10^{-15} erg cm^{-2} s^{-1})			1.7 ± 0.1		
Knot1 region						
Soft comp.	EM[c] (10^{10} cm^{-5})	$2.5^{+2.2}_{-1.8}$	$1.6^{+1.1}_{-0.6}$	$1.3^{+0.6}_{-0.4}$	$1.8^{+0.4}_{-0.3}$	$1.2^{+0.4}_{-0.3}$
	kT_e (keV)	$0.30^{+0.05}_{-0.07}$	0.43 ± 0.10	$0.57^{+0.14}_{-0.10}$	0.51 ± 0.05	$0.69^{+0.16}_{-0.12}$
	n_et (10^{9} cm^{-3} s)	4.8	$8.8^{+12.0}_{-1.9}$	$7.5^{+1.9}_{-1.4}$	$7.9^{+1.3}_{-1.0}$	$7.6^{+2.7}_{-1.5}$
	abundance			fixed to the solar value		
Reference comp.[d]	EM[a] (10^{9} cm^{-5})	$2.4^{+1.0}_{-0.9}$	$1.4^{+0.7}_{-0.3}$	$2.3^{+1.0}_{-0.9}$	$2.9^{+1.1}_{-1.0}$	$5.2^{+2.4}_{-2.1}$
Power law	Γ			2.79 (linked to Ref1)		
	Flux[b] (10^{-15} erg cm^{-2} s^{-1})			1.7 (linked to Ref1)		
χ^2 (d.o.f.)				731 (629)		

Notes.
[a] EMs for the NEI components are defined as $\int n_e n_{\rm C} dV/(4\pi d^2[{\rm C/H}]_\odot)$.
[b] The energy flux in the energy band of 4–6 keV.
[c] EMs for the soft components are defined as $\int n_e n_{\rm H} dV/4\pi d^2$.
[d] The parameters of the reference components other than the EMs are linked to the NEI component for the Ref1 region.

2000 cannot be determined because of a lack of statistics. We thus fixed n_et in 2000 to that in 2003 minus 4×10^9 cm^{-3} s (=42 cm^{-3} × 3 yr). Note that fixing n_et does not change the other parameters beyond the 1σ confidence level. The EMs of the Ref1 component are free parameters, and the other parameters are linked to those for the Ref1 spectra.

It may be possible that the uncertainty of n_et in 2000 is caused by contamination of X-rays from the SW. We thus investigate a possibility of an extension of the SW emission by checking a spectrum of an inner region of Knot1 toward the SW (the Ref2 region in Figure 2). Figure 5 shows the Ref2 spectra and the models whose parameters except for EM are fixed to those of Ref1. As can be seen from the figure, the Ref2 spectra do not have the soft-band excess like those of Knot1. The result shows that the SW extension is negligible and that the soft thermal emission comes only from Knot1.

The spectra of Knot1 and the result of the spectral fit are presented in Figures 4(b)–(f). The best-fit parameters are listed in Table 2. We confirm that the time variability can be ascribed solely to the additional soft component. Since the NEI model with the solar abundance can reproduce the Knot1 spectra in the soft band well, the soft component can be attributed to ISM heated up by the blast wave. To further clarify the variability, we plot kT_e, n_et, and EM as a function of time in Figure 6. We also show the parameters when n_et is a free parameter in the figure. kT_e increases significantly from $0.30^{+0.05}_{-0.07}$ to $0.69^{+0.16}_{-0.12}$ keV in 2000–2015. As can be seen from the figure, kT_e in both cases are almost equal. We also confirm the kT_e change when n_et is fixed to 8×10^9 cm^{-3} s, which is between the best-fit value (9×10^{10} cm^{-3} s) and the fixed value (4×10^9 cm^{-3} s). In this case, kT_e in 2000, 2003, 2007, 2009, and 2015 are $0.47^{+0.20}_{-0.28}$, $0.42^{+0.10}_{-0.04}$, $0.59^{+0.13}_{-0.10}$, $0.53^{+0.03}_{-0.06}$, and $0.70^{+0.14}_{-0.13}$ keV, respectively.

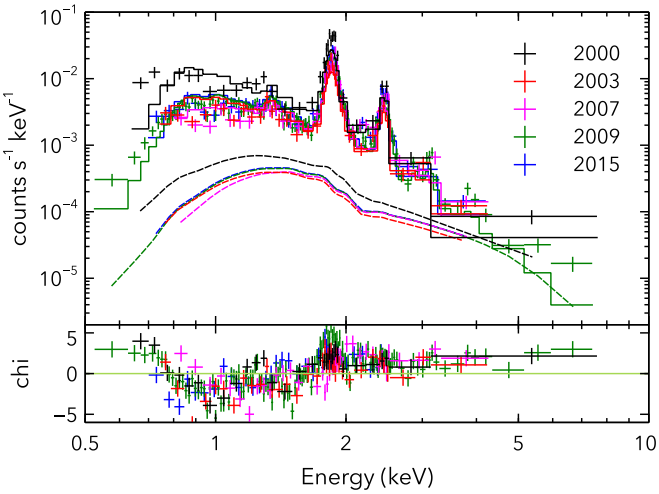

Figure 5. The spectra and the best-fit model of Ref2 taken in 2000 (black), 2003 (red), 2007 (magenta), 2009 (green), and 2015 (blue). The lines show the model whose parameters, except for EM, are fixed to those of Ref1. The components represent the same ones as Figure 4.

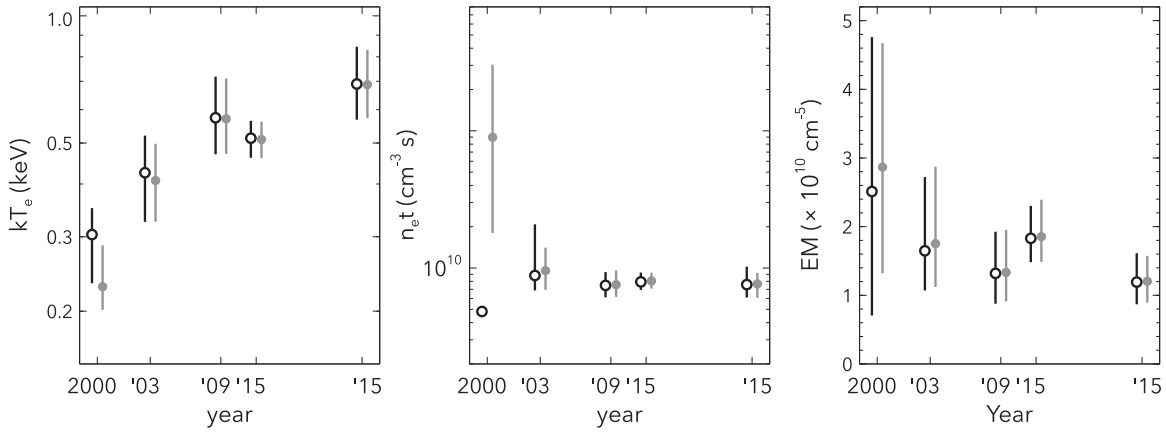

Figure 6. Time variations of kT_e (left), n_et (middle), and EMs (right) of the best-fit soft component of Knot1. The black and gray plots represent the best-fit parameters when n_et is fixed and free, respectively.

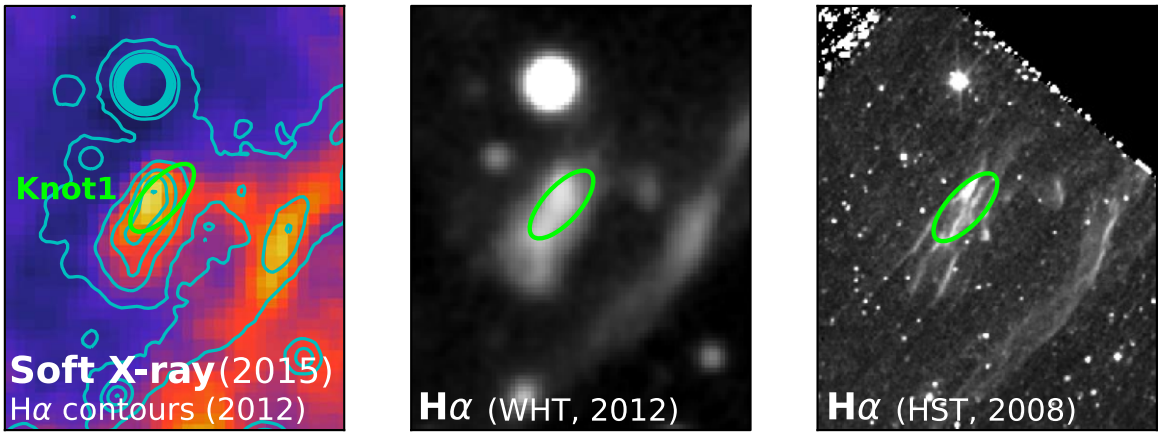

Figure 7. Left: soft-band Chandra image taken in 2015 (same as the rightmost panel of Figure 2) overlaid with contours of an Hα image taken in 2012 (see the middle panel). Middle: Hα image obtained in 2012 with GHαFaS on the William Herschel Telescope (WHT; Knežević et al. 2017). Right: Hα image taken in 2008 with WFPC2 on HST (Lee et al. 2010).

Based on the kT_e increase, we also model the soft component with `gnei`, an NEI model in which the ionization timescale averaged temperature is not required to be equal to the current temperature. The value of kT_e of `gnei` are $0.26^{+0.07}_{-0.05}$, $0.37^{+0.09}_{-0.07}$, $0.57^{+0.13}_{-0.10}$, $0.52^{+0.05}_{-0.07}$, and $0.70^{+0.17}_{-0.13}$ keV in 2000, 2003, 2007, 2009, and 2015, respectively; they are almost the same as those of the NEI model. We find no notable changes in n_et and EM over time. We can interpret that the observed flux change is due to an increase of electron energy caused by the shock heating.

4. Discussion

4.1. Origin of Knot1

As described in Section 3, the significant increase of the soft-band X-ray flux is seen in Knot1 in Tycho. Together with the year-scale increase of the electron temperature, the result implies that a compact dense clump was recently heated by the blast wave. The model with the solar abundance reproduces the spectra, suggesting that the shock-heated gas is of ISM origin (Table 2). We do not, however, rule out the possibility of the circumstellar medium (CSM) origin since the southwestern shell is known to be interacting with a cavity wall (Tanaka et al. 2021). Note that Knot1 is the first example of ISM/CSM X-ray emission in the ejecta-dominated SNR, Tycho. Future observations with improved statistics will enable us to measure the abundance of each element, resulting in a determination of its true origin. It may also hint at the progenitor system of Tycho's Type Ia SN.

In the northeastern region, previous Hα observations (Kirshner et al. 1987) revealed Balmer-dominated filaments, which are interpreted as radiation from a forward-shocked neutral gas and shock precursors (e.g., Ghavamian et al. 2000; Lee et al. 2007). Figure 7 (the left and middle panels) shows a comparison between the soft-band X-ray image taken in 2015 and the Hα image taken in 2012 (Knežević et al. 2017). We find that a bright Hα structure spatially coincides with Knot1 in X-rays. This finding supports the ISM/CSM origin of Knot1.

We point out that the bright and complicated shell structure is seen only around Knot1 in the entire Hα image of the northeastern part of Tycho taken with the Hubble Space Telescope (HST; the right panel of Figure 7 and see Lee et al. 2010). Similar localized multiple filaments are present in other SNRs; the "XA" region, the southwestern limb of the Cygnus Loop (Hester & Cox 1986; Graham et al. 1995), and an ejecta knot of Cas A (Patnaude & Fesen 2007, 2014). In the case of Cas A, time variability of thermal X-rays was detected in a physical scale of 0.02–0.03 pc, which roughly agrees with the estimated size of Knot1: $\simeq$0.04 pc. These structures are considered as dense clumps engulfed by the blast waves. We thus infer that Knot1 originated from a small-scale clumpy ISM/CSM heated by the forward shock.

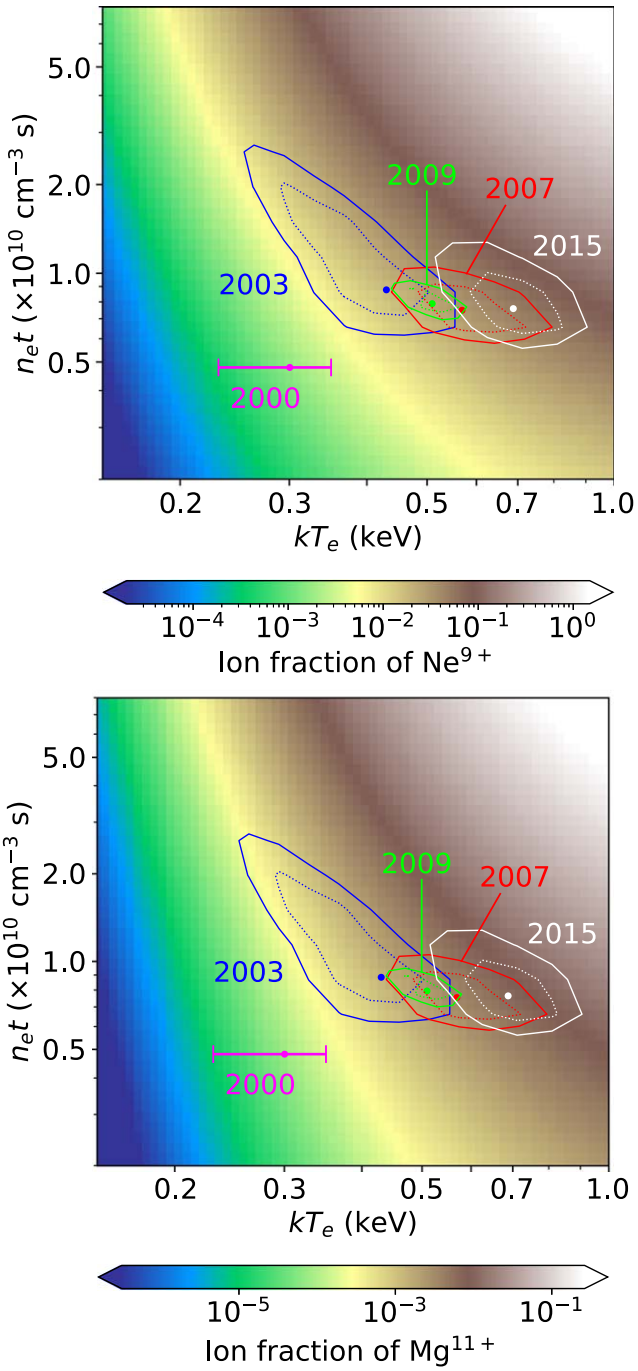

Figure 8. Ion fractions of Ne^{9+} (top) and Mg^{11+} (bottom), i.e., H-like ions as a function of kT_e and $n_e t$. The dotted and solid line contours show $\Delta\chi^2 = 1.0$ and 2.3 confidence levels, respectively, in 2003 (blue), 2007 (red), 2009 (green), and 2015 (white). The points represent the best-fit parameters in each year. For 2000 data, we show only the uncertainty of kT_e since $n_e t$ was fixed in our analysis (see the text).

Here we estimate the density of Knot1 using the best-fit parameters as follows. Assuming that the emitting region of Knot1 has an oblate-spheroidal shape with long and short radii of 0.05 pc and 0.02 pc, respectively, we obtain its volume of $V \simeq 6 \times 10^{51}$ cm^3. From the best-fit parameter of the soft component in 2015, the emission measure is $n_e n_H V/4\pi d^2 = (1.2^{+0.4}_{-0.3}) \times 10^{10}$ cm^{-5}, from which we derive a proton density of $n_H = 35^{+6}_{-4}$ cm^{-3}. Since the postshock density of Tycho is estimated to be $n_H = 0.1$–2 cm^{-3} from the flux ratio of the 70 to 24 μm infrared emission (Williams et al. 2013), the small clump in Knot1 has roughly 10–100 times higher density than the surroundings.

4.2. Time Variability of Knot1

4.2.1. Cloud Crushing Time

Since the parameter $n_e t$ in XSPEC represents the ionization timescale assuming constant kT_e, it is not reasonable, when kT_e is significantly increasing, to consider $n_e t$ as a product of density and actual time passed. In order to discuss the change in ionization state of Knot1, we calculated ion fractions of the soft component in each year. As shown in Figure 8, H-like Ne and Mg are both increasing, supporting that the ionization has progressed from 2003 to 2015. We thus consider that Knot1 is heated and ionized year to year by an SNR shock recently propagating into a small cloud.

To estimate the timescale for shock heating, we assume ram pressure equilibrium ($\rho_i u_i^2 \simeq \rho_c u_c^2$), where ρ and u are the density and the velocity, respectively, in ISM (subscript i) and inside the clump (subscript c). The velocity of the shock decelerated inside the clump is described as

$$u_c = \frac{u_i}{\chi^{1/2}}. \quad (1)$$

Here, χ ($\equiv \rho_c/\rho_i$) is the density contrast between the clump and the ISM. Assuming $\chi = n_c/n_i \simeq 10$ following the discussion in Section 4.1 and that the forward-shock velocity (u_i) is typical of Tycho (4000–8000 km s^{-1}; Tanaka et al. 2021), we obtain $u_c = 1500$–2500 km s^{-1}.

Following the discussion by Patnaude & Fesen (2014), we define a cloud crushing time:

$$t_{cc} \equiv \frac{\chi^{1/2} a_0}{u_i} = \frac{a_0}{u_c}, \quad (2)$$

where a_0 is the radius of the clump (Klein et al. 1994). Since the radius of the X-ray emitting region of Knot1 is $a_0 \simeq 0.02$ pc, the cloud crushing time is $t_{cc} = 18 \times (u_i/2000\ \mathrm{km\ s^{-1}})^{-1}$ yr. We point out that the result is roughly consistent with the year-scale change of the X-ray flux in Knot1.

4.2.2. Heating Timescale

To explain the observed increase of kT_e in Knot1, we first assume a thermal equilibration via ion–electron Coulomb collisions without collisionless heating at the shock transition region. The immediate downstream temperature for a shock velocity u_c is written as

$$kT_i = \frac{3}{16} m_i u_c^2, \quad (3)$$

where m_i is the mass of particle species i. Since the electron temperature (T_e) is lower than the ion temperature (T_i) in the downstream plasma, a simple increase of T_e is expected, and its time evolution is described as

$$\frac{dT_e}{dt} = \frac{T_i - T_e}{t_{eq}}, \quad (4)$$

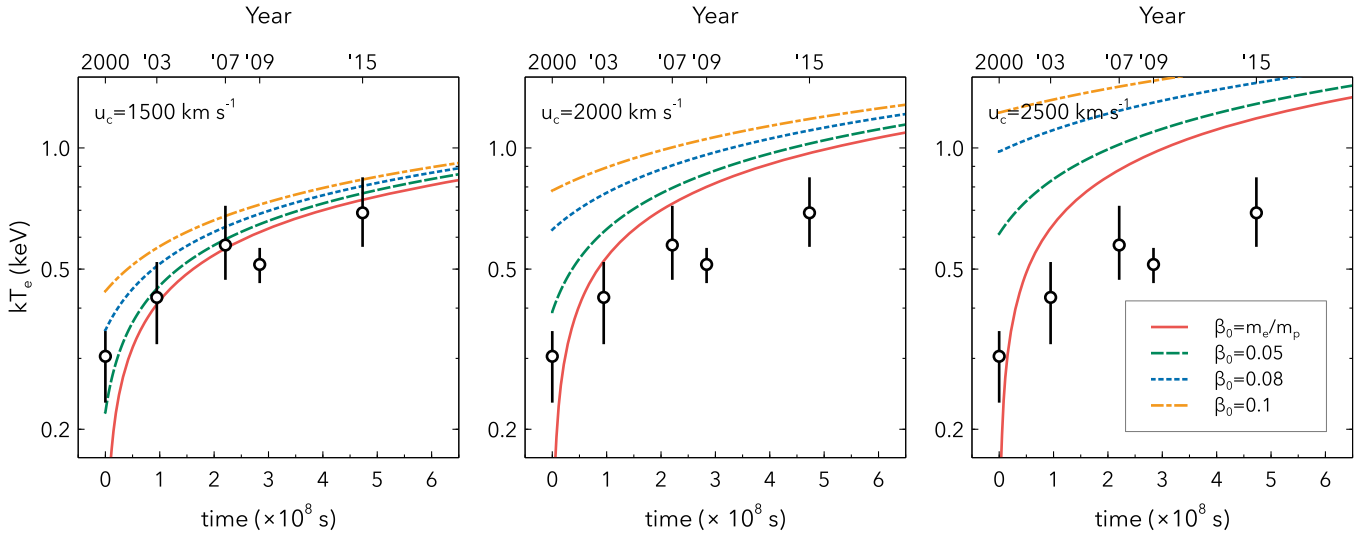

Figure 9. Best-fit results of kT_e for Knot1 (same as the left panel of Figure 6) and calculated time variations with assumptions of $u_c = 1500$ km s^{-1} (left), 2000 km s^{-1} (middle), and 2500 km s^{-1} (right). The solid, dashed, dotted, and dashed–dotted lines represent cases of $\beta_0 = m_e/m_p \simeq 1/2000$, 0.05, 0.08, and 0.1, respectively.

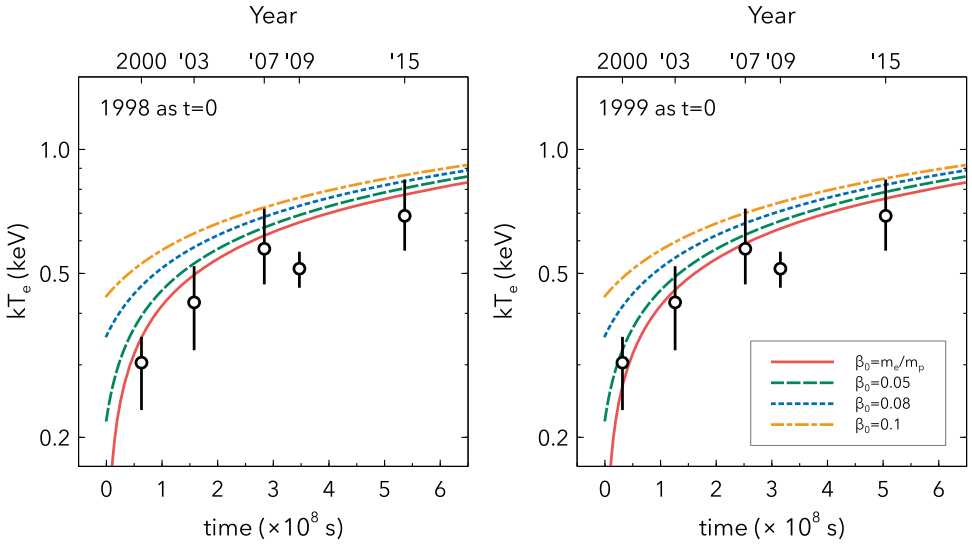

Figure 10. Same as Figure 9, but assuming the years 1998 (left) and 1999 (right) as $t = 0$ in the case of $u_c = 1500$ km s^{-1}.

where the equilibration timescale t_{eq} is given by the following expression (Spitzer 1962; Masai 1984):

$$t_{eq} = \frac{3m_e m_i k^{3/2}}{8(2\pi)^{1/2} n Z_i^2 e^4 \ln\Lambda}\left(\frac{T_e}{m_e} + \frac{T_i}{m_i}\right)^{3/2}$$
$$\ln\Lambda = 24.8 + \ln\left[\left(\frac{kT_e}{\mathrm{eV}}\right)\left(\frac{n_e}{\mathrm{cm}^{-3}}\right)^{-1/2}\right]. \quad (5)$$

Here, Z_i and e are the charge number and the elementary charge, respectively. We take the electron number density $n_e = 42$ cm^{-3} under the assumption of $n_H = 35$ cm^{-3} (Section 4.1) and $n_e = 1.2 n_H$. Assuming no contributions from ions heavier than hydrogen for simplicity, kT_e evolves as shown in Figure 9. If only Coulomb collisions are considered, the electron-to-proton temperature ratio ($\beta_0 \equiv T_e/T_p$) at $t = 0$ should be equal to the mass ratio of the particles, i.e., $\beta_0 = m_e/m_p \simeq 5 \times 10^{-4}$. From Figure 9, we find that the model for $u_c = 1500$ km s^{-1} can explain the result.

When the collisionless process is effective at the shock transition (e.g., Cargill & Papadopoulos 1988; Laming 2000; Ghavamian et al. 2007), the ratio β_0 should be larger than m_e/m_p ($\simeq 5\times10^{-4}$). We try $\beta_0 = 0.05$, 0.08, and 0.1 as plotted in Figure 9. The model with $m_e/m_p \leqslant \beta_0 \leqslant 0.05$ agrees well with the data. Since we do not know when the forward shock will indeed hit Knot1, we compare several calculations with different assumptions about $t = 0$ in the case of $u_0 = 1500$ km s^{-1} in Figure 10. Even in the case of the year 1998 as $t = 0$, $m_e/m_p \leqslant \beta_0 \leqslant 0.05$ is still possible, but the year 1999 as $t = 0$ is more plausible.

While the shock velocity u_c plausibly ranges from 1500 to 2000 km s^{-1} as estimated in Section 4.2.1, the kT_e trend may indicate a lower u_c than 1500 km s^{-1}. Figures 11 and 12 show calculated time variations of kT_e in the case of $u_c \leqslant 1000$ km s^{-1}. The observed kT_e can be roughly explained for $m_e/m_p \leqslant \beta_0 \leqslant 0.15$. If this slower u_c is the case, the density contrast χ might be larger or the forward-shock velocity u_i might be slower than expected, which should be constrained by future observations.

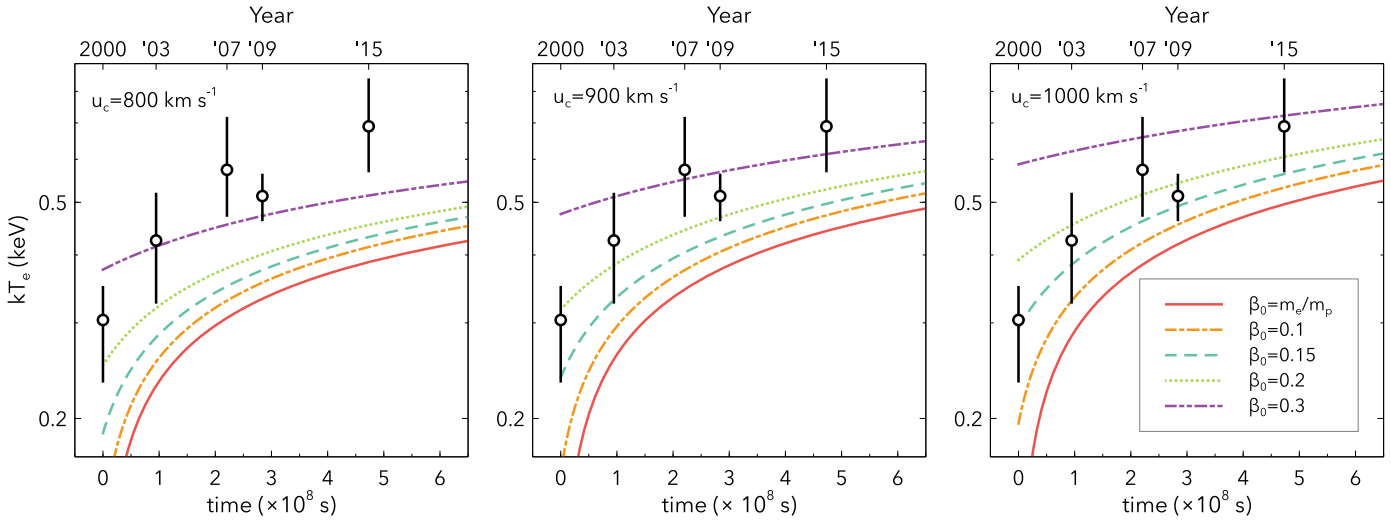

Figure 11. Best-fit results of kT_e for Knot1 (same as the left panel of Figure 6) and calculated time variations with assumptions of $u_c = 800$ km s^{-1} (left), 900 km s^{-1} (middle), 1000 km s^{-1} (right). The solid, dashed–dotted, dashed, dotted, and dashed–dotted–dotted lines represent cases of $\beta_0 = m_e/m_p \simeq 1/2000$, 0.1, 0.15, 0.2, and 0.3, respectively.

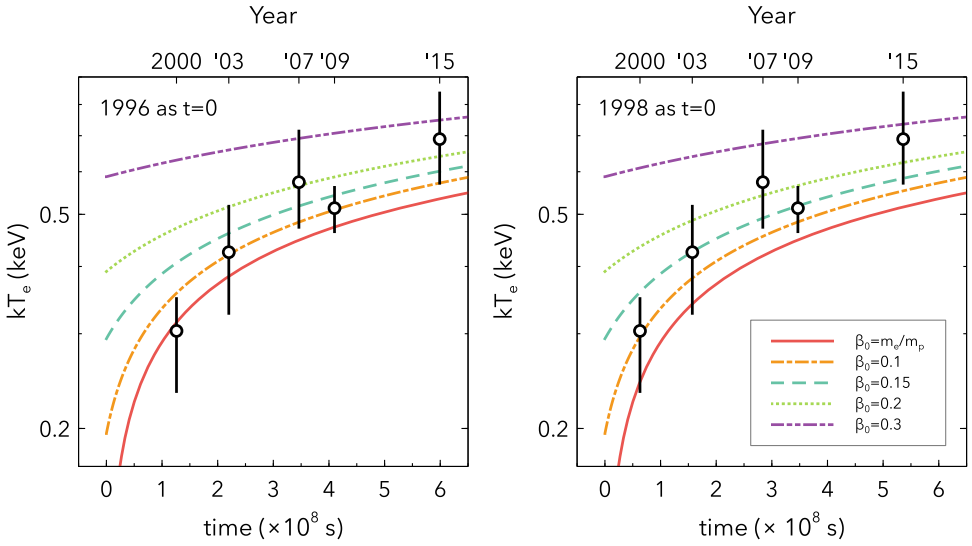

Figure 12. Same as Figure 11, but assuming the years 1996 (left) and 1998 (right) as $t = 0$ in the case of $u_c = 1000$ km s^{-1}.

Based on the flux ratios of the broad-to-narrow components of the Hα line, β_0 is estimated for some SNRs with different shock velocities (e.g., van Adelsberg et al. 2008). In Tycho, Ghavamian et al. (2001) and van Adelsberg et al. (2008) obtained $\beta_0 < 0.1$ and $\beta_0 = 0.046^{+0.007}_{-0.006}$, respectively, in a well-known region "knot g," located $\sim 2'$ southeast of Knot1. Other SNRs such as SN 1006 and Kepler's SNR, which have strong shocks with $v_{\rm sh} > 1000$ km s^{-1}, have $\beta_0 \sim 0.05$ (Fesen et al. 1989; Ghavamian et al. 2002). On the other hand, β_0 is greater than 0.1 in SNRs with slow shocks ($v_{\rm sh} \leqslant 1000$ km s^{-1}), e.g., Cygnus Loop, RCW 86 (Ghavamian et al. 2001), and SNR 0548−70.4 (Smith et al. 1991). Knot1 has $m_{\rm e}/m_{\rm p} \leqslant \beta_0 \leqslant 0.05$ in a shock velocity of about 1500 km s^{-1}, or $m_{\rm e}/m_{\rm p} \leqslant \beta_0 \leqslant 0.15$ in a shock velocity of about 1000 km s^{-1}, which is consistent with these previous studies. It indicates that Knot1 has collisionless electron heating with efficiency comparable to the result of the Hα observation.

5. Conclusion

We searched for a short timescale variability of thermal X-ray radiation in Tycho, using the Chandra X-ray Observatory data in 2000, 2003, 2007, 2009, and 2015. We discovered a significant brightening of a compact emission in the northwestern limb (Knot1). Our spectral analysis indicated that the time variability of Knot1 was due to a change of the electron temperature kT_e of forward-shocked gas. Knot1 was the first detection of shock-heated ISM/CSM in this remnant. The best-fit result indicated a gradual increase of kT_e from $0.30^{+0.05}_{-0.07}$ to $0.69^{+0.16}_{-0.12}$ keV of Knot1 during 2000–2015. From these results, together with localized multiple Hα filaments in Knot1, we considered that a small ($\simeq$0.04 pc in diameter) dense ($n_{\rm H} \sim 30$ cm^{-3}) clump was recently encountered by the forward shock. By calculating equilibration timescales of kT_e, β_0 ($\equiv T_e/T_p$) was required to be $m_{\rm e}/m_{\rm p} \leqslant \beta_0 \leqslant 0.05$ when shock velocity

is 1500 km s^{-1} and $m_e/m_p \leqslant \beta_0 \leqslant 0.15$ when shock velocity is 1000 km s^{-1} to reproduce the observed change in the electron temperature. Our result shows the collisionless heating in Knot1, which has comparable efficiency to the previous Hα observations of knot g in Tycho and the other SNRs with high shock velocities.

We thank Dr. Sladjana Knežević for providing the WHT Hα image. We acknowledge the anonymous referee for useful comments and suggestions that improved the quality of this paper. This research has made use of data obtained from the Chandra Data Archive and software provided by the Chandra X-ray Center (CXC) in the application package CIAO. This work is supported by JSPS KAKENHI Scientific Research grant Nos. JP21J20027 (M.M.), JP19K03915, JP22H01265 (H. U.), JP19H01936 (T.T.), JP22K18721, JP22H04572 (T.G.T.), and JP21H04493 (T.G.T. and T.T.).

Facility: CXO, CXOING:Herschel (GHαFaS).

Software: CIAO (Fruscione et al. 2006), XSPEC (Arnaud 1996), SAOImageDS9 (Joye & Mandel 2003).

ORCID iDs

Masamune Matsuda https://orcid.org/0000-0002-7393-2234
Hiroyuki Uchida https://orcid.org/0000-0003-1518-2188
Takaaki Tanaka https://orcid.org/0000-0002-4383-0368
Hiroya Yamaguchi https://orcid.org/0000-0002-5092-6085
Takeshi Go Tsuru https://orcid.org/0000-0002-5504-4903

References

Arnaud, K. A. 1996, in ASP Conf. Ser. 101, Astronomical Data Analysis Software and Systems V, ed. G. H. Jacoby & J. Barnes (San Francisco, CA: ASP), 17
Borkowski, K. J., Reynolds, S. P., Williams, B. J., & Petre, R. 2018, ApJ, 868, L21
Cargill, P. J., & Papadopoulos, K. 1988, ApJL, 329, L29
Cassam-Chenaï, G., Hughes, J. P., Ballet, J., & Decourchelle, A. 2007, ApJ, 665, 315
Fesen, R. A., Becker, R. H., Blair, W. P., & Long, K. S. 1989, ApJL, 338, L13
Foster, A. R., Smith, R. K., & Brickhouse, N. S. 2017, in AIP Conf. Ser. 1811, Atomic Processes in Plasmas (APiP 2016) (Melville, NY: AIP), 190005
Fruscione, A., McDowell, J. C., Allen, G. E., et al. 2006, Proc. SPIE, 6270, 62701V
Ghavamian, P., Laming, J. M., & Rakowski, C. E. 2007, ApJL, 654, L69
Ghavamian, P., Raymond, J., Hartigan, P., & Blair, W. P. 2000, ApJ, 535, 266
Ghavamian, P., Raymond, J., Smith, R. C., & Hartigan, P. 2001, ApJ, 547, 995
Ghavamian, P., Winkler, P. F., Raymond, J. C., & Long, K. S. 2002, ApJ, 572, 888
Graham, J. R., Levenson, N. A., Hester, J. J., Raymond, J. C., & Petre, R. 1995, ApJ, 444, 787
Hester, J. J., & Cox, D. P. 1986, ApJ, 300, 675
Hwang, U., Decourchelle, A., Holt, S. S., & Petre, R. 2002, ApJ, 581, 1101
Joye, W. A., & Mandel, E. 2003, in ASP Conf. Ser., 295, Astronomical Data Analysis Software and Systems XII, ed. H. E. Payne, R. I. Jedrzejewski, & R. N. Hook (San Francisco, CA: ASP), 489
Kirshner, R., Winkler, P. F., & Chevalier, R. A. 1987, ApJL, 315, L135
Klein, R. I., McKee, C. F., & Colella, P. 1994, ApJ, 420, 213
Knežević, S., Läsker, R., van de Ven, G., et al. 2017, ApJ, 846, 167
Laming, J. M. 2000, ApJS, 127, 409
Laming, J. M., Raymond, J. C., McLaughlin, B. M., & Blair, W. P. 1996, ApJ, 472, 267
Lee, J.-J., Koo, B.-C., Raymond, J., et al. 2007, ApJL, 659, L133
Lee, J.-J., Raymond, J. C., Park, S., et al. 2010, ApJL, 715, L146
Markevitch, M., Govoni, F., Brunetti, G., & Jerius, D. 2005, ApJ, 627, 733
Masai, K. 1984, Ap&SS, 98, 367
Matsuda, M., Tanaka, T., Uchida, H., Amano, Y., & Tsuru, T. G. 2020, PASJ, 72, 85
McKee, C. F. 1974, ApJ, 188, 335
Miceli, M., Sciortino, S., Troja, E., & Orlando, S. 2015, ApJ, 805, 120
Okuno, T., Tanaka, T., Uchida, H., et al. 2020, ApJ, 894, 50
Patnaude, D. J., & Fesen, R. A. 2007, AJ, 133, 147
Patnaude, D. J., & Fesen, R. A. 2014, ApJ, 789, 138
Ravi, A. P., Park, S., Zhekov, S. A., et al. 2021, ApJ, 922, 140
Russell, H. R., McNamara, B. R., Sanders, J. S., et al. 2012, MNRAS, 423, 236
Rutherford, J., Dewey, D., Figueroa-Feliciano, E., et al. 2013, ApJ, 769, 64
Sato, T., & Hughes, J. P. 2017, ApJ, 840, 112
Schwartz, S. J., Thomsen, M. F., Bame, S. J., & Stansberry, J. 1988, JGR, 93, 12923
Smith, R. C., Kirshner, R. P., Blair, W. P., & Winkler, P. F. 1991, ApJ, 375, 652
Spitzer, L. 1962, Physics of Fully Ionized Gases (New York: John Wiley and Sons, Inc.)
Sun, L., Vink, J., Chen, Y., et al. 2021, ApJ, 916, 41
Tanaka, T., Okuno, T., Uchida, H., et al. 2021, ApJL, 906, L3
Uchiyama, Y., & Aharonian, F. A. 2008, ApJL, 677, L105
Uchiyama, Y., Aharonian, F. A., Tanaka, T., Takahashi, T., & Maeda, Y. 2007, Natur, 449, 576
van Adelsberg, M., Heng, K., McCray, R., & Raymond, J. C. 2008, ApJ, 689, 1089
Warren, J. S., Hughes, J. P., Badenes, C., et al. 2005, ApJ, 634, 376
Williams, B. J., Borkowski, K. J., Ghavamian, P., et al. 2013, ApJ, 770, 129
Wilms, J., Allen, A., & McCray, R. 2000, ApJ, 542, 914
Yamaguchi, H., Eriksen, K. A., Badenes, C., et al. 2014, ApJ, 780, 136
Yamaguchi, H., Hughes, J. P., Badenes, C., et al. 2017, ApJ, 834, 124
Zhou, P., Chen, Y., Zhang, Z.-Y., et al. 2016, ApJ, 826, 34